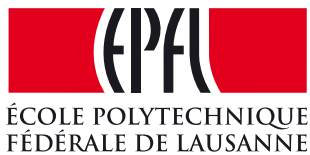


## RESEARCH PLAN

### **Atomistic modeling of solid–liquid interface of metals and alloys out of equilibrium**



ÉCOLE POLYTECHNIQUE  
FÉDÉRALE DE LAUSANNE

**Candidate:** Edoardo Baldi

**Thesis director:** Prof. Michele Ceriotti

Laboratory of Computational Science and Modeling  
École Polytechnique Fédérale de Lausanne

Lausanne, EPFL

June 21, 2016



# Contents

<b>1</b>	<b>Additive manufacturing</b>	<b>1</b>
1.1	Introduction to Additive Manufacturing . . . . .	1
1.2	Manufacturing processes . . . . .	2
1.3	Materials . . . . .	4
1.4	Present challenges . . . . .	16
<b>2</b>	<b>Simulating additive manufacturing</b>	<b>19</b>
2.1	Present simulation approaches . . . . .	19
2.2	Focus on interfacial properties . . . . .	21
2.3	Capillary fluctuations and free energies . . . . .	23
<b>3</b>	<b>The capillary fluctuation method revisited</b>	<b>27</b>
3.1	The method . . . . .	27
<b>4</b>	<b>Modeling atomistic interactions</b>	<b>33</b>
4.1	The embedded atom method . . . . .	33
4.2	Applications to alloys . . . . .	35
	<b>Bibliography</b>	<b>39</b>



# 1 Additive manufacturing

## 1.1 Introduction to Additive Manufacturing

The term “additive manufacturing” (AM) can be considered as an evolution of the “rapid prototyping” process, used in various industries to indicate a process of rapidly creating a system or part of it before the final release and commercialization (i.e. a prototype). However, recently a significant improvement in the output of these processes has shown that there is a much closer link with the final product and the new name of “additive manufacturing” has been chosen.

In few words, the basic feature of the AM technology is the possibility to design an object of interest by means of a 3D Computer Aided Design (CAD) software and then fabricate it directly with almost no need of process planning. Though a very complicated process, AM has the advantage to significantly simplify the work of producing complex 3D objects directly from a software project. Other manufacturing process would require a detailed analysis of the object to determine, for example, the order in which each part has to be built and also the assembly phase.

The key principle to understand how AM works is that the object is built layer by layer, where each layer is a thin cross-section of the object itself derived from the CAD data. However, in real world, each layer must have a finite thickness and so the resulting object will only be an approximation of the original (virtual) project.

At its early stage, AM was used to build visualization models for products as they were being developed. From this initial purpose, AM technology greatly improved as knowledge of materials used and accuracy of the process improved as well. When AM is used in conjunction with other technologies to form a process chain, it can significantly reduce times and costs. Furthermore, the possibility to use high-power lasers has meant that desired objects can be directly made in a broad variety of materials, particularly metals and related ones, thus extending the application range.

AM technologies have been described as a very revolution in product development and manufacturing. Moreover, results obtained with AM suggest that this technology could actually redefine what we mean today by a “manufacturing process”. In order to (try to) explain these enthusiastic forecasts, we need to remark what are the advantages of AM technologies. First, we should emphasize again the “rapid” character of this process: it is not just in term of time needed to built an object, but all the development

process experiences a speedup, mainly because we are using computers throughout. This is possible thanks to the fact that the transfer from the virtual project to the AM machine is relatively seamless and does not require nearly any interpretation of the design intent (i.e. knowing what functionality the object should have, which influences the way it has to be built).

Not least important is the reduction of the number of process steps. Despite the possible complexity of objects to be built, an AM process is usually performed in one single step; other manufacturing processes would require a particular sequence of multiple and/or iterative steps to be carried out and even a relatively simple change in the project may require significant modification in the fabrication process and, in turn, the time required increases.

### 1.2 Manufacturing processes

As opposed to conventional machining processes, based essentially on material removal, AM relies on the idea of “material incremental manufacturing”. Thus, a typical AM process involves a number of steps which can lead from the virtual description of the object to the physical resultant one.

Starting from the CAD model of the object to produce, the second step is converting the virtual data to a format accepted by the AM machine; nearly every AM apparatus can read from a file format known as STL (“STereo Lithography”), in which the original CAD model is represented in terms of its external surfaces. Transferring virtual data to the machine also means to ensure that the object has the correct size, position and orientation for building. Then, a setup phase must be done: such settings relate to the building parameters like materials characteristics, energy source, layer thickness and timings. The next step is the real building phase, which is mainly an automated process. Lastly, the object has to be removed from the machine and sometimes it may require a “post-processing phase” before it can be ready to use.

The current research focus of AM techniques is to produce complex shaped functional metallic components, including metals, alloys and metal matrix composites in order to meet the demanding requirements of several important industrial sectors, such as aerospace, biomedical and rapid tooling. For this class of applications, AM components are actually used as real production parts, with particular microstructural and mechanical properties. For the fabrication of these components to be cost effective and as accurate as possible, three typical laser based processes have been developed: these are *laser sintering* (LS), *laser melting* (LM) and *laser metal deposition* (LMD). Since a variety of metals and related materials can be processed, these AM techniques are regarded as the most versatile. However, laser based AM generally involves complex out-of-equilibrium physical and chemical metallurgical process, in which heat and mass transfer can occur in different modes [1, 2], sometimes together with chemical reactions [3, 4]. The complex metallurgical phenomena that occur during AM processing are both strongly material and process dependent. Therefore, gaining a deeper and more detailed understanding of the out-of-equilibrium transformation the material

undergoes is necessary to have more control on methods of laser processing, in order to achieve the desired microstructural and mechanical properties of the resultant product. Although all laser additive manufacturing processes share the same philosophy of incremental manufacturing, each techniques has its specific characteristics in terms of which materials can be used and processing details (e.g. laser type). We shall now briefly underline some interesting aspects about LS and LM techniques, with a more in-depth focus on the latter as it is the main manufacturing process we are interested in.

### 1.2.1 Laser sintering

Firstly, we can distinguish LS and the other two techniques (LM, LMD) by the fact that the latter imply a complete melting of the powder during the process, while with the former the powder undergoes only a partial melting. As a consequence, powder to be processed with LS must have more than one constituent and each with a different melting point. The multicomponent powder mixtures are typically composed of an high melting point metallic component as the structural metal and a low melting point metallic component as a binder. In contrast with pure metal powders, prealloyed powders exhibit temperature range where both solid and liquid phases coexist during the process; as laser parameters are optimized, the optimal temperature should be within this range. Densification and consolidation of this semisolid system occur as a results of the rearrangement of particles still in the solid phase by the influence of the capillary forces exerted by the liquid phase.

### 1.2.2 Laser melting

With *laser melting* (also known as *selective laser melting*) the powder, be it a pure metal or an alloy, is brought far above the melting point. The full melting is made possible by the improvement in laser processing conditions, such as higher laser energy, smaller spot size, reduced layers thickness. One considerable step ahead of LM is the possibility to process also pure non-ferrous metals, such as Ni, Ti, Cu, Al<sup>1</sup> which cannot be well processed with LS mainly due to their high viscosity.

Currently, LM is used to manufacture functional prototypes and to build up final parts directly. The tool and mould-making industry is a typical example of a branch producing final parts in small batches. Thanks to its almost infinite geometrical freedom, LM is applied to manufacture tooling inserts with particularly complex shapes that would require too many steps with a traditional technique.

Medical technology is another field exploiting the possibility of building through LM an object with almost any conceivable shape. Examples are hip implants or surgical instruments out of titanium alloys as well as dental restorations out of cobalt chromium. Some known drawbacks of LM are the requirement of an high power laser as source and the fact that thin powder layer thickness requires longer building times. Moreover,

---

<sup>1</sup> Actually, aluminum is subject to other issues related to its high reflectivity and known susceptibility to oxidation.

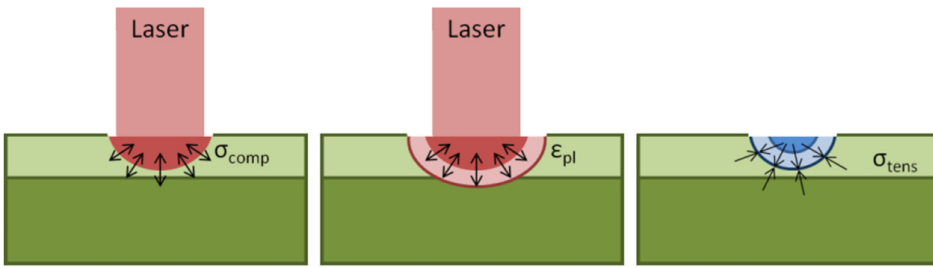


Figure 1.1 – Schematic picture showing the temperature gradient mechanism leading to crack formation and subsequent delamination of the part [5].

as the powder completely melts and then solidifies again, a large degree of thermal deformation is possible, thus leading to the accumulation of stresses in the resultant products. The high temperature gradients which the processed part undergoes during the laser interaction are substantially responsible of crack formation and delamination of produced parts [5] (Fig. 1.1). These problems are especially prevalent in ceramic materials. Ceramics require very high melting temperatures and have very low thermal conductivity, resulting in very high thermal gradient during the process. Combined with its low fracture toughness, ceramics present a difficult challenge to be used as a material processed through LM.

Another relevant issue typical of LM is the phenomenon called *balling*: it happens when molten metal forms spheroidal beads due to poor wetting of the preceding layer, which in turn is caused by surface tension. Balling is an obstacle to the formation of continuous melt lines, leading to rough and bead-shaped surfaces. In more severe cases, balling may aggravate subsequent layers formation and cause LM to literally "jam" the powder coating mechanism resulting in large metallic drops that extend above the powder bed [6]. Das and Kruth [7] have explained that the formation of oxide film on a layer impedes effective bonding with the subsequent one. This is mainly due to the fact that oxide films show poor wettability with respect to liquid metals in absence of a chemical reaction. One possible solution to this phenomenon is carrying out the manufacturing process under protective atmosphere, using high purity inert gases.

### 1.3 Materials

All the additive manufacturing technique described above can be applied, on theoretical grounds, to metallic materials in any form as well as to other classes of materials (see Fig. 1.2). For the purposes of this report, we shall limit the discussion to two classes: pure metals and alloys powder. In the last part of this section, we describe in a more detailed way three specific metal alloys of particular interest to companies we collaborate with.

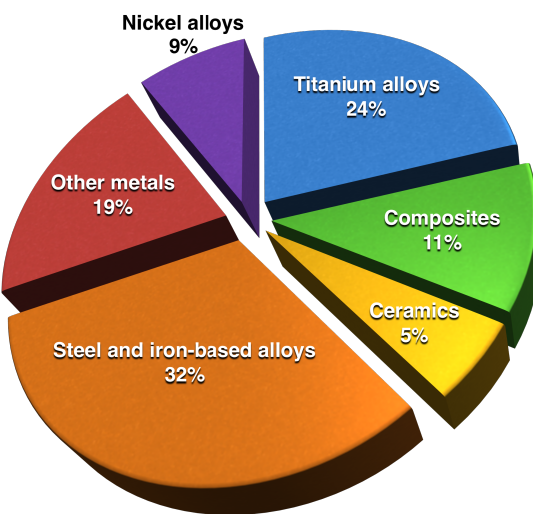


Figure 1.2 – Research interests on LM manufacturing of different materials, based on publications indexed by Web Of Science and ScienceDirect from 1999 to 2014. From [6].

### 1.3.1 Common classes of materials

#### Pure metals

Pure metals have been applied for various AM processes since the beginning. However, they are no more the focus of future development of AM technology mainly because of two reasons: firstly, pure metals are known to have relatively poor mechanical properties and, from a chemical point of view, they are more prone to corrosion and/or oxidation. Secondly, early attempts to processing pure metals with the laser sintering technique have been largely unsuccessful (i.e. poor overall quality of final products) and a real improvement has been possible only with first successful applications of LM. For example [8], LS processing of pure Ti samples showed that final products typically has an heterogeneous microstructure, which consists of cores of unmelted powder grains, melted surface of grains and residual voids; this means that the density of parts so obtained can be quite far from the level required to ensure good mechanical properties. For these reasons, currently industrial applications moved from LS to LM or LMD to build nonferrous pure metals components. It is worth noting, however, that recent studies [9, 10] on a partial melting mechanism of pure metals such as Ti and Ta have demonstrated the interesting possibility of producing complex shaped porous structures with functionally graded porosity used for biomedical applications.

#### Alloys powder

The majority of the actual research (and subsequent applications) has been focused on powder alloys, based on metals such as Ti, Ni and Fe. Additive manufacturing of aluminum-based alloys might be the next research step, in order to face the difficulties related to the processing of nonferrous alloys with high reflectivity to laser energy. Almost all the work on AM of alloys powder is based on a complete melting mechanism,

thus adopting the techniques of LS or LMD. Therefore, high laser source power is generally required to yield good bonding mechanism and obtain fully dense parts (excepts for porous materials if needed). Examples of lasers used for this purpose are CO<sub>2</sub> powered lasers, Nd:YAG and fibre lasers. Besides the setup of the processing parameters, residual stresses and microstructures are two important aspects to take into account, as they are strongly influenced by large undercooling degree during rapid solidification, after the laser source has generated the molten pool. As proposed by Abe et al. [11], a possible way to solve these issues is the use of a dual laser scanning system; essentially, in this way one of the two laser can be used during a "preheating" phase before the actual melting or after the latter in a "reheating" phase.

### 1.3.2 Nickel based superalloys

A superalloy is a metallic alloy which can be used at high temperatures, often in excess of the absolute melting temperature. Resistance to creep and oxidation are the design criteria of prime interest. Superalloys can be based on iron, cobalt or nickel, with the latter being widely studied as best suited many industrial, high-performance applications such those required in the aerospace field.

The fundamental solutes in nickel based superalloys are aluminium and titanium, with a total concentration which is typically less than 10 atomic percent. This generates a two-phase equilibrium microstructure, consisting of gamma ( $\gamma$ ) and gamma-prime ( $\gamma'$ ) phases. It is the  $\gamma'$  which is largely responsible for the elevated temperature strength of the material and its incredible resistance to creep deformation. The amount of  $\gamma'$  depends on the chemical composition and temperature.

The  $\gamma$  phase is a solid solution with a Face Centered Cubic lattice and a random distribution of the different species of atoms. By contrast,  $\gamma'$  has a simple cubic lattice in which the nickel atoms are at the face-centres and the aluminium or titanium atoms at the cube corners, as the following picture shows schematically.

This atomic arrangement has the chemical formula Ni<sub>3</sub>Al or Ni<sub>3</sub>Ti. However, as can be seen in the following phase diagram at 1573 K, from the ( $\gamma+\gamma'$ )/ $\gamma'$  phase boundary on the ternary sections of the Ni, Al, Ti the phase is not strictly stoichiometric: there may exist an excess of vacancies on one of the sublattices which leads to deviations from stoichiometry or substitutional defects may be present, i.e. some of the Ni atom may occupy Al sites or vice-versa.

One of the most important properties of these alloys is their strength up to very high temperatures. More precisely, these alloys show high yield strengths (usually denoted by  $\sigma_y$ ) and at first these values are independent on temperature. An explanation of this peculiar property lies in the structure of the two phases: both have a cubic lattice with similar lattice parameters and the  $\gamma$  phase forms the matrix in which the  $\gamma'$  precipitates. In this "transition" cubic symmetry is preserved and thus cell edges of the  $\gamma'$  are exactly parallel to the corresponding edges of the  $\gamma$  phase. Furthermore, because their lattice parameters are similar, when the precipitate size is small, there is a little lattice misfit between the two phases . Dislocations in the  $\gamma$  nevertheless find it difficult to penetrate

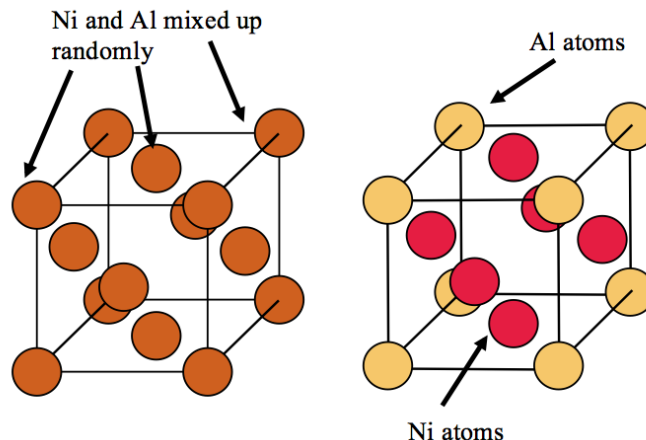


Figure 1.3 – On the right, the structure of the  $\gamma$  phase, a solid solution of Ni and Al atoms. The left scheme is the structure of the  $\gamma'$ . From: <http://www.eng-atoms.msm.cam.ac.uk/>

$\gamma'$ , partly because the latter is an atomically ordered phase. The order interferes with dislocation motion and hence strengthens the alloy.

Also the mismatch between the lattice parameters of the two phases plays quite an important role: it promotes the stability of the microstructure at high temperature. This is mainly due to the fact that the  $\gamma$  and the  $\gamma'$  belong to almost equal crystal structure and thus the  $\gamma/\gamma'$  interface energy is quite low. The mechanism of precipitate coarsening (i.e. the Oswald ripening) is thermodynamically driven by the minimisation of the interface energy and therefore the more coherent is the interface (i.e. the smaller its surface free energy), the more stable is the microstructure, because especially at high temperature it does not happen that a precipitate of a solid phase grows at the expense of another one.

Commercial superalloys contain more than just Ni, Al or Ti. Essential resistance to oxidation is promoted also by the presence of chromium besides aluminum and small quantities of yttrium help the oxide layer to be commensurate with the substrate. Furthermore, when dealing with polycrystalline superalloys the addition of boron and zirconium results in reducing the grain boundary energy, which in turn improves overall creep strength. There are, naturally, limits to the concentrations of these elements that can be added without inducing precipitation or promoting the formation of brittle phases.

### 1.3.3 Titanium alloys

Titanium alloys are among the most important of the advanced materials that are essential in several fields of applications, from aerospace to biomedical. This is because of an excellent combination between mechanical properties and, for example, a formidable resistance to corrosion exhibited by titanium alloys. On the other hand, the high cost of production of these alloys compared to competing materials is one of the main reasons

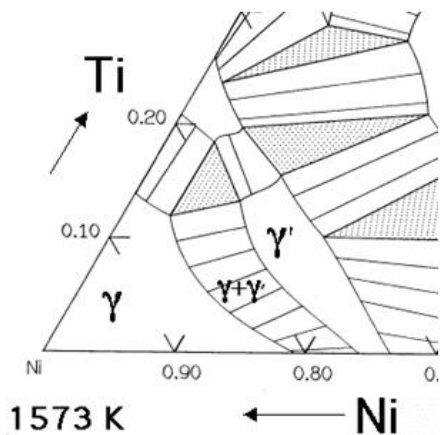


Figure 1.4 – Ni-Al-Ti ternary phase diagram at 1573 K with the  $\gamma$ ,  $\gamma'$  and coexistence regions indicated. From From: <http://www.eng-atoms.msm.cam.ac.uk/>

negating their widespread use.

Like a number of other metals titanium can crystallize in various crystal structures. The complete transformation from one into another crystal structure is called “allotropic transformation”.

Pure titanium, as well as the majority of titanium alloys, crystallizes at low temperatures in a modified ideally hexagonal close packed structure, called  $\alpha$  titanium. At high temperatures, however, the body-centered cubic structure is stable and is referred to as  $\beta$  titanium. The  $\alpha - \beta$  transition temperature for pure titanium is 882 °C. The atomic unit cells of the hexagonal close packed (hcp)  $\alpha$  titanium and the body-centered cubic (bcc)  $\beta$  titanium are schematically shown in Fig. 1.5 with their most densely packed planes and directions highlighted. The existence of the two different crystal structures and the corresponding allotropic transformation temperature is of central importance since they are the basis for the large variety of properties achieved by titanium alloys. Depending on their influence on the  $\beta$  transition temperature, the alloying elements of titanium are classified as neutral,  $\alpha$ -stabilizers, or  $\beta$ -stabilizers (Fig. 1.6). The  $\alpha$ -

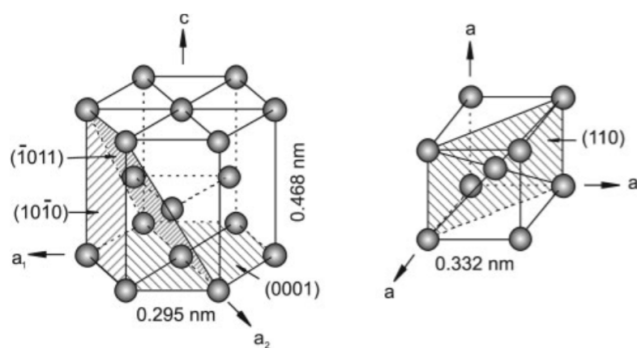


Figure 1.5 – Crystal structure of HCP  $\alpha$  and BCC  $\beta$  phase [12].

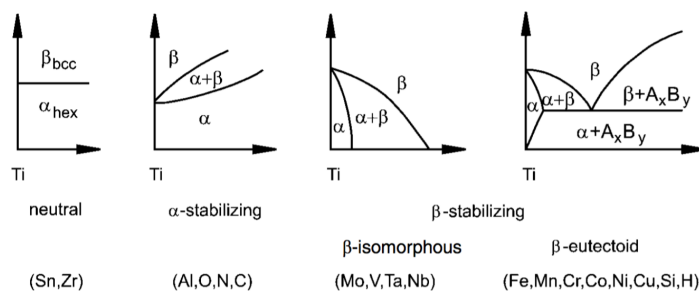


Figure 1.6 – Schematic picture of the influence of alloying elements on Ti phase diagrams [12].

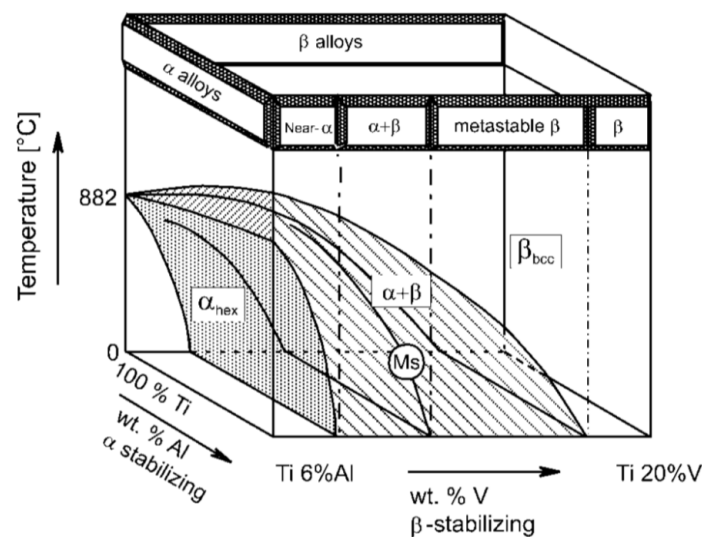


Figure 1.7 – Three-dimensional phase diagram to classify Ti alloys [12].

stabilizing elements extend the  $\alpha$  phase field to higher temperatures, while  $\beta$ -stabilizing elements shift the  $\beta$  phase field to lower temperatures. Neutral elements have only minor influence on the transition temperature. Apart from the regular alloying elements, there are also primarily nonmetallic elements on the order of few 100 ppm present as impurities.

Among the  $\alpha$ -stabilizers, aluminum is by far the most important alloying element of titanium. The interstitial elements oxygen, nitrogen, and carbon also belong to this category. In addition to extending the  $\alpha$  phase field to higher temperatures, the  $\alpha$ -stabilizers develop a two-phase  $\alpha + \beta$  field.  $\beta$ -stabilizing elements are subdivided into  $\beta$ -isomorphous and  $\beta$ -eutectic elements. Of these, the  $\beta$ -isomorphous elements such as Mo, V, and Ta are by far more important due to their much higher solubility in titanium. In Fig. 1.7 a schematic three-dimensional diagram shows the most stable phases with respect to the added concentration of stabilizers (here only Al and V are shown).

The microstructure of conventional titanium alloys is primarily described by the size and

arrangement of the two phases  $\alpha$  and  $\beta$ . The two extreme cases of phase arrangements are the lamellar microstructure, which is generated upon cooling from the  $\beta$  phase field, and the equiaxed microstructure, which is a result of a recrystallization process. Both types of microstructure can have a fine as well as a coarse arrangement of their two phases. Generally, the different microstructures are generated by thermomechanical treatments, considered as a complex sequence of solution heat treatment, deformation, recrystallization, aging, and annealing for stress relief.

An important point for thermomechanical treatment is the  $\beta$ -transition temperature ( $T_\beta$ ), since it separates the single  $\beta$  phase field from the two-phase  $\alpha + \beta$  field. Lamellar microstructures are a result of simple cooling from temperatures above  $T_\beta$ . Once the temperature falls below the  $T_\beta$ ,  $\alpha$  phase nucleates at grain boundaries and then grows as lamellae into  $\beta$  grains. Depending on the cooling rate, the lamellae are either fine or coarse: slow cooling from the  $\beta$  phase field results in pure lamellar microstructures, with the lamellae becoming coarser with reduced cooling rate. Rapid quenching, instead, leads to a martensitic transformation of the  $\beta$  phase, resulting in a very fine needle-like microstructure.

To generally improve the properties of materials, and titanium alloys in particular, there are essentially two ways to proceed: alloying and processing. Recently a third option has gained importance: the production of composite materials.

Alloying lays the basis for an increase in strength (e.g. solid-solution strengthening, age hardening), allows the generation of ordered structures (e.g. intermetallic compounds of titanium and aluminum), determines most of the physical properties (e.g. density, elastic modulus, coefficient of thermal expansion), and largely controls the chemical resistance of the material (corrosion, oxidation).

Processing allows the careful balancing of the property profile of materials. Depending on the specific property profile required for the final application, different microstructures can be generated for titanium alloys by means of thermomechanical treatment to optimize for strength (solid solution strengthening, dispersion strengthening, grain boundary strengthening, texture hardening), ductility, toughness, superplasticity, stress corrosion, creep resistance, etc. The processing techniques of rapid solidification and mechanical alloying extend the spectrum of potential alloy compositions.

### 1.3.4 Gold alloys

Gold is an element with one of the most unique spectrum of properties and for this reason its use is particularly widespread, not only for luxury goods like jewelry, but also in many other technical applications despite its high price. From the chemical point of view it is the most “noble” of all metals: it does not corrode or oxidize and its stability towards influences from a variety of external conditions (be it natural, biomedical or technical) persists up to high temperatures. Moreover, it possesses high electrical and thermal conductivity and, from a mechanical point of view, is very soft, highly malleable and ductile at room temperature. Also optical properties play a crucial role for its applications: in its pure form gold shows a rich yellow color, but gold alloys

can be made to assume a range of colours by varying the alloying additions. Human history is rich in examples of the usage of gold and its colours for different purposes. In almost all areas of application, however, gold cannot be used in its pure form. It needs to be alloyed with other elements, usually metals, to adjust specific properties. For most applications, pure gold is simply too soft. For several applications, the properties of the pure gold need to be maintained as much as possible, for example, bonding wires in electronics or high carat gold jewelry<sup>2</sup>.

The starting point for any kind of metallurgical processing not only for gold is provided by phase diagrams. The most common and used binary and ternary alloys of gold have been extensively studied and reviewed [13–15]. In this section we try to give a summary of the metallurgical approaches of gold alloying adopted in many fields of applications, with particular focus to grain refinement and solution strengthening.

### Grain refinement

Grain refinement or grain-size control is the fundamental process applied routinely to all industrial applications of gold alloys. The list of advantages of a fine-grained material over a coarse-grained one is long and well documented:

- increase of strength, malleability and ductility, as well as work-hardening effectiveness during cold-working process;
- increase of chemical homogeneity due to less pronounced alloying elements segregation. This in turn has a positive impact on corrosion resistance and susceptibility to embrittlement and crack formation in casting processes;
- an improvement of surface characteristics and finishing properties, mainly of interest for decorative and jewelry applications.

The only disadvantage provided by fine-grained material occurs at high temperatures where a loss of strength and reduction of creep resistance, due to a change of prevailing deformation mechanisms.

Grain-size control during material processing involves two particularly important steps: **solidification** after melting and **annealing** after cold-working.

Grain refinement during solidification mainly is concerned with promoting the formation of a larger number of nuclei for crystal growth from the molten state. This can be achieved by additions of particular elements with higher melting points with respect to the metal and low solubility in solid gold, such as iridium, ruthenium and rhenium, to cite a few [16]. The required amount of the additions depends on alloy composition and can vary between 50 and 1000 ppm. Higher amounts are not meaningful, since no further grain refining effect is usually observed.

Grain refining additions usually are introduced via carefully prepared base metal master alloys, for example Cu–10% Ir, which need to offer a good liquid and solid

---

<sup>2</sup>Caratage is defined as the fraction of pure gold present in a certain alloy. That is: 24 carat gold (24kt) = 100 wt% Au, while Xkt = (X × 100)/24 wt% Au.

solubility for the grain refiner, to provide a homogeneous distribution in the master alloy.

Apart from alloy additions, grain size during solidification is also influenced by processing [17]. Cold pouring of molten metal is frequently applied, keeping both metal and mould at low temperatures. This enhances crystal nucleation and retards crystal growth, leading to more fine-grained castings. Mould agitation or vibration support the homogeneous distribution of nuclei and “mechanically” refine the structure by breaking up the branches (dendrites) of growing crystals.

During cold-working processes, the microstructure of a metal becomes strongly distorted: the material is strengthened and ductility is reduced to very low levels after heavy deformation. Complete or partial annealing then is carried out to recover ductility. For sufficiently high annealing temperature and time, the material recrystallizes, which involves nucleation and growth of new grains of regular shape.

Grain refinement during the annealing stage after deformation is mainly based on two mechanisms: increase of the number of recrystallization nuclei in the deformed microstructure and, more importantly, the decrease of grain growth velocity. For gold alloys, some of the additions that have been mentioned above as grain refiners during solidification can also promote the formation of recrystallization nuclei. However, if the growth of the nuclei is not inhibited as well, the described mechanism alone does not necessarily lead to a fine-grained microstructure. In extreme cases it may even have an adverse effect on grain size, namely if excessive growth of a few number of preferentially formed nuclei occurs. Furthermore, a fine-grained recrystallized structure energetically is not stable and tends to coarsen during prolonged annealing. For all these reasons, the decrease of grain growth velocity by specific alloying additions is always of high importance. Impurities as well as alloying additions with low solubility in the metal matrix can reduce the grain boundary mobility drastically [18, 19], because they tend to segregate to grain boundaries and therefore need to be able to move together with them during recrystallization and grain growth. This requires time and temperature-dependent diffusion processes to occur, which slows down recrystallization and grain growth kinetics.

### Strengthening mechanisms

Deformation of any metal takes place by the sliding of crystal planes over each other through the movement of dislocations. Any distortion of the crystal lattice or any obstacle in the lattice increases the force required to move the dislocations through the lattice. Hence this leads to an increase of hardness or strength but usually also to a decrease of deformability. Figure 1.8 gives an overview of the hardness increase in binary gold alloys depending on the type and amount of alloying element added.

The largely different dependencies are related to the different prevailing strengthening mechanisms, as well as the particular microstructural condition the material is in. Among these mechanisms, we mention: *solid solution hardening*, *order-disorder transformation hardening* and *precipitation hardening*.

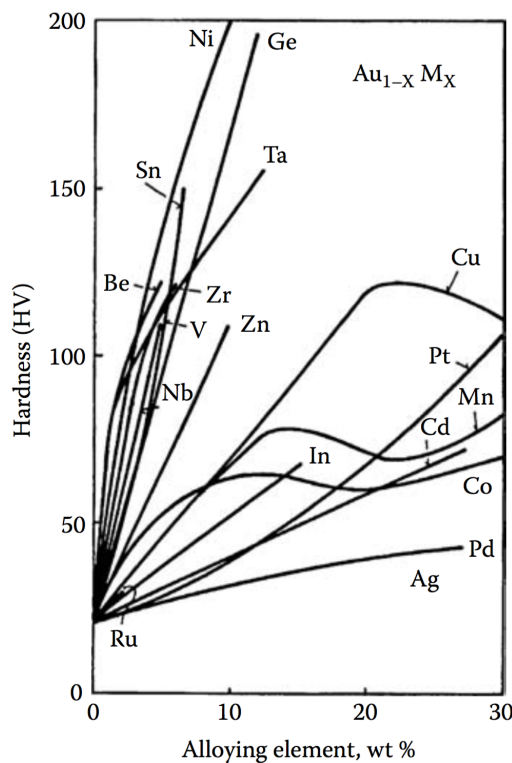


Figure 1.8 – Hardness trends in binary gold alloys depending on the type and amount of addition in weight % [20]. Units on hardness are expressed according to the “Vickers hardness test”, that is:  $\text{HV} = \text{force}/\text{area} = [\text{k}\text{gf}]/[\text{mm}^2]$ .

The last two mechanisms are reversible processes, since the material can be brought back to the “nonhardened” state by a homogenization heat treatment. These mechanisms are also usually referred to as *age hardening*.

For the sake of completeness, we also cite the irreversible mechanism of *dispersion hardening*, which is based on the irreversible formation of finely dispersed particles, mainly oxides (but also carbides or borides), by reaction of alloying elements with oxygen (or carbon/boron). This often involves special processing routes like internal oxidation or powder metallurgy.

**Solid solution hardening.** This mechanism involves dissolution of alloying elements in solid gold, which can either replace gold atoms in the crystal lattice (as substitutional defects) or can fill in the small gaps between gold atoms in the crystal lattice (interstitial solid solution hardening).

The effect of solid solution hardening increases with the extent of lattice distortion associated with an alloying addition; thus the larger is the difference in atomic size between the host metal and the added element, the more prominent is this effect. This partially explains qualitatively the dependence of hardness on the Ag-Cu ratio in the

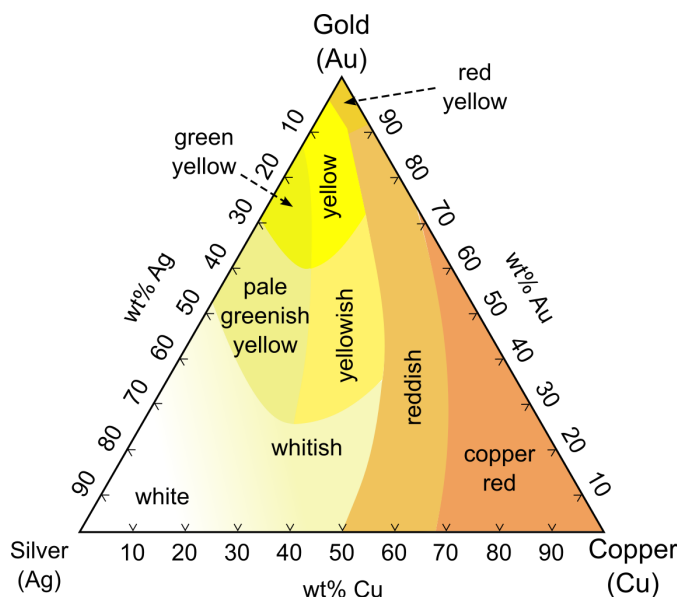


Figure 1.9 – Approximate colours of Au–Ag–Cu alloys, which are commonly used in jewelry making. From Wikimedia.

Au–Ag–Cu ternary system, which forms the basis for many common jewelry (mainly for gold “color spectrum”, Fig. 1.9) and dental alloys.

Gold is only slightly larger than silver, while copper atoms are  $\sim 12\%$  smaller than gold: this explains why Cu is more effective in strengthening of gold by substitutional solid solution. On the other hand, Ag is completely soluble in Au at all temperatures and for any composition, while Cu is only miscible down to  $\sim 410\text{ }^\circ\text{C}$ : below this point, some intermetallic phases form, which give rise to additional hardening effects by precipitation hardening. Besides Ag and Cu, also palladium and platinum (soluble at any composition only at high temperatures) are largely used to induce solid solution strengthening. However, similarly to Ag, the strengthening effect of Pd and Pt is only small or moderate and usually further treatments are necessary to obtain the alloy with desired properties.

**Order-disorder transformation hardening.** Due to the lowering of temperature during alloy processing, the atoms can arrange themselves in an ordered solid solution (also referred to as intermetallic compounds or intermediate phases), where different atoms occupy strictly defined lattice sites. Here strengthening is caused by the related elastic distortions, but also because the movement of dislocations is considerably more difficult because the ordered state needs to be preserved.

In the Au–Cu system, the intermediate phases responsible of this mechanism are CuAu, CuAu<sub>3</sub> and Cu<sub>3</sub>Au. The most important one is the phase occurring below 410 °C at the composition for which the ratio Au:Cu is 1: alternating layers of Au and Cu form a face-centered tetragonal phase (AgCu I) stable below 385 °C, while an orthorombic phase is stable between 385 °C and 410 °C (AgCu II). When Au:Cu ratio approaches 1:3,

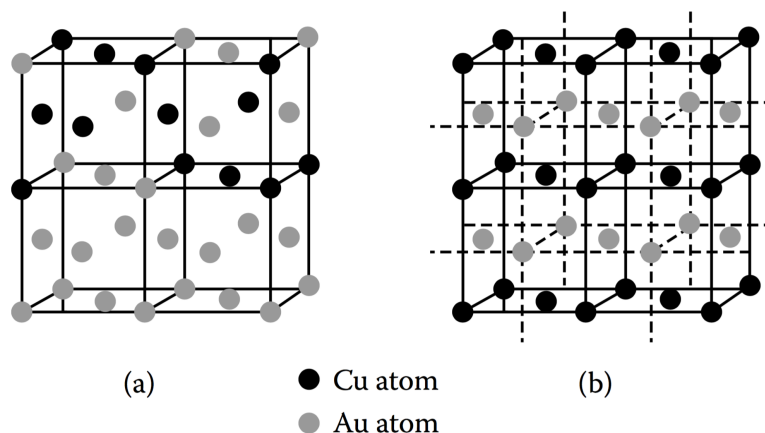


Figure 1.10 – (a) Crystal structure of the disordered solid solution in FCC AuCu. (b) Crystal structure of the ordered face-centered tetragonal phase, AgCu [23].

two versions of  $\text{AuCu}_3$  form with another ordered face-centered cubic symmetry (Cu atoms on lattice faces and Au atoms on lattice edges).

This hardening mechanism is a very important feature for many carat gold jewelry [21] and dental alloys [22]. It can be obtained either by slow cooling from high temperatures or by an aging period in the temperature range between 150 and 400 °C.

**Precipitation hardening.** The prerequisite for the activation of this mechanism is the reduced solid solubility of an alloying element in the metal matrix. Solid solubility generally decreases with temperature, thus this class of alloying elements can be precipitated by particular heat treatment as finely dispersed particles.

For binary gold alloys, this is the case of Au with Co, Cr, Fe, Mn and many others [13]. It can occur for several reasons:

- the system behaves as a series of solid solutions at high temperatures, but as temperature decreases a miscibility gap opens up for certain compositions. This is the case of the Au-Ni, Au-Pt systems;
- systems in which a limited mutual solubility is present over the whole temperature range, like Au-Co and Au-Cr;
- alloy systems that present similar features as above, but where more than one intermetallic phase can occur.

Of course, also in more complex systems, like ternary or quaternary alloys, this hardening mechanism can occur. In all the cases, the system is subject to both a heat treatment and an aging period, which should comprise the following steps:

1. an homogenization phase useful to dissolve all the alloying elements in the gold matrix. For the example systems mentioned above, this means a temperature between 700 and 900 °C for several hours depending on the actual composition;

2. rapid quenching from the temperature of the previous step, to suppress the formation of precipitates. Up to this phase, the alloying elements remain dissolved in the crystal lattice (in a sort of “supersaturated” solid solution);
3. an aging period at low temperatures (200–400 °C) that can span from minutes to several hours, depending on the composition and other factors.

Analysis of precipitation hardening phenomena is possible through high resolution electron microscopy, which often reveals that shape, composition and crystal structure of precipitates change with the aging time; thus the last step of the aforementioned schematic recipe for strengthening by precipitation is usually a complex multistage effect. Lastly, prolonged aging almost always leads to coarsening and coalescence of the precipitates and a related hardness drop, a phenomenon that is referred to as overaging by Ostwald ripening.

### 1.4 Present challenges

Issues related to the techniques described in previous sections can be divided in two different, though linked, fields: the first one is from a material science perspective and a second one related to technological-industrial aspects.

General physical properties of materials that are fundamental to all laser-based manufacturing processes are absorptance, surface tension (and wettability) and viscosity: these are to be taken into account when thinking of design strategies of the target product.

Among more specific aspects of AM that are presently subject to study, there are microstructural and mechanical properties and the out of equilibrium phenomenon known as solute trapping. The first two are of primary importance for AM applications and, at the same time, they represent quite broad classes of materials properties. Solute trapping is of peculiar interest when studying solid–liquid interfaces. Therefore, we try to give here a concise, but detailed, overview of these features.

Mechanical properties of AM processed components are strongly linked to the solidification microstructure. The high-energy laser interaction gives rise to a very fast heating and melting of materials, which is inevitably followed by a rapid solidification on cooling. Laser-based AM processes normally offer high heating and cooling rates ( $\sim 100 \text{ K/s}$ )<sup>3</sup> at the solid–liquid interface, producing a molten pool of quite small size ( $\sim 1 \text{ mm}$ )<sup>4</sup>. Furthermore, the rates of quenching that occur by conduction of heat through the substrate are fast enough to produce a rapid solidification microstructure. Therefore, as a characteristic of AM processed materials, grain refinement is generally expected, due to an insufficient time for grain development and growth. Moreover, either chemical concentration or temperature gradients in the molten pool may generate surface tension gradient, making the solidification a non-steady state process (due to the so-called “Gibbs–Marangoni effect”). On the other hand, rapid solidification has

---

<sup>3</sup>ref. 166 Gu book

<sup>4</sup>ref. 167 Gu book

the kinetic limitation of crystal growth that normally follows the direction of maximum heat flow. The simultaneous but competitive action of the above two mechanisms, i.e. a non-equilibrium solidification nature and a localized directional growth tendency, may lead to a variety of crystal orientations with a short-range regularity [24]. Therefore, metallic materials processed by AM may present intrinsic, more or less, anisotropic features.

Another important issue concerning mechanical properties of AM-processed materials is related to the residual stresses (i.e. stresses that remain inside a material, when it has reached equilibrium with its environment) that arise in the parts being produced. Residual stresses may impose some serious limitations to the practical use, since they introduce part deformations and/or micro cracks. Moreover, large residual stresses can limit the load resistance of the parts compared to a stress-free state.

In general, residual stresses are considerably large in parts fabricated in a layer-by-layer fashion. A thorough theoretical and experimental study by Kruth et al. [25] has disclosed that the residual stress profile consists of two zones of large tensile stresses at the top and bottom of a processed part and a large zone of intermediate compressive stress in between. The magnitude and shape of the residual stress profile depend on the geometric height of the part, the material properties and laser scanning strategy and processing conditions.

Among material properties the elastic modulus and the coefficient of thermal expansion play an important role in what determines the level of residual stresses.

The elastic modulus is of primary importance when phase transformations take place, as they may be detrimental or beneficial with respect to residual stresses. Normally, the formation of brittle phases during AM may promote stress cracking, whereas some controlled phase transformations may have the potential to reduce or eliminate stresses and deformation.

Laser processing conditions can be tuned to control the presence of residual stresses. For LS and LM processes, the laser scanning strategy has a significant influence on the residual stresses being developed. Normally, the stresses are larger perpendicular to the scan direction than along the scan direction [26] and a subdivision of the surface in smaller sectors has been shown to lead to a lower stress value.



## 2 Simulating additive manufacturing

### 2.1 Present simulation approaches

As a whole, AM processes are considered as an important step-change in manufacturing technologies nowadays widely used, opening up the possibility of going almost directly from Computer Aided Design to net-shape defined products. With sufficient penetration in the industrial sector, this kind of technology could have a significant impact on both the environment and on sustainable manufacturing, with large reduction of material wastage and integrated components with specific optimized features. However, there are many challenges to be overcome to increase the importance of these technologies for the industry. These range for business considerations to technical and inherent differences in the processes from industry standards.

Computational modeling has a relatively important role to play in addressing these issues, when compared with its role in other manufacturing processes. An interesting aspect of AM from the perspective of computational modeling regards the manufacturing length scales. In a conventional casting process, for example, the local cooling rates are determined on a macroscale, thus directly linked to the size of the casting. All the phenomena occurring during such a process usually spread across a broad length scale, making a multi-scale simulation approach a rather challenging task. On the other hand, the manufacturing length scales of powder through AM processes are much smaller and closely related to the size of the melt pool; also, solidification cooling rates are much higher. Thus, in a multi-scale simulation, the linking across the length scales could be more achievable by common modeling techniques such as finite elements or phase field simulations, both of which can guide the fabrication process to obtain components with designed features (e.g. microstructures, mechanical properties, etc.). With the aid of computational modeling, there are several key areas which are subject of research interests, namely:

- thermal modeling of melting and solidification;
- residual stress modeling;
- topological and shape optimization of components.

Among these topics, the first one regarding the fundamental phenomena of melting and solidification is by far the most important. Also, analysis of residual stresses has its starting point with the thermal history of the processed component. Besides meso-scale approaches useful to bridge the gap between the modeling phase and actual industrial fabrication, also simulation techniques at the atomic scale can give valuable insights when trying to better understand complicate processes of AM.

There are several motivations to employ atomistic simulations to study materials under the conditions they are subject to during AM processes. The foremost reason is related to the out-of-equilibrium conditions that are usually the “scenario” in which additive manufacturing takes place: we already mentioned the importance of this kind of phenomena that occur away from thermodynamical equilibrium (see Section 1.4). Thus, atomistic simulations are the most predictive method to investigate these aspects.

Furthermore, there are some general physical properties that are in common with all AM techniques and atomistic simulations serve as a versatile tool to study in depth all of these properties. In this particular context, “general” physical properties means studying: viscosity (and the closely related diffusion coefficient), absorptance and the class of solid–liquid interface properties. We shall discuss these properties briefly in the last part of this section.

### Viscosity and diffusion coefficient

Viscosity and diffusion coefficient are strictly related (e.g. by the Stoke–Einstein relation). Both of these properties are of relevant importance for AM, and especially laser–driven manufacturing: viscosity of the melt pool is required to be low enough such that it successfully spreads on the previously processed layer. According to Takamichi and Roderick, for a process like LM in which the powder system undergoes a complete melting, the dynamic viscosity of the liquid can be defined as [27]

$$\eta = \frac{16}{15} \sqrt{\frac{m}{k_B T}} \gamma \quad (2.1)$$

where  $\gamma$  is the surface tension of the liquid (all the other quantities being self-explanatory). This viscosity decreases with increasing the working temperature, which in turn leads to better diffusion properties of the liquid in conjunction with solid particles and, eventually, an improved densification. An issue can be met when processing metallic system with a strong formation tendency of intermetallic compounds, which are generally brittle and may increase the viscosity of the melt.

### Absorptance

AM processes generally involve direct interaction of metallic powders with laser beam. The study of absorptance properties of powders is particularly important because it allows one to determine the suitable “processing window”, which, in the best case scenario, should be free of a non-response of powder due to insufficient laser energy

and material evaporation due to excessive input power. The absorptance<sup>1</sup> is defined as the ratio of the absorbed radiation to the incident radiation. As opposed to dense materials, only a fraction of the incident radiation is absorbed by the outer surface of particles; another part of the radiation penetrates through the interparticles voids.

Absorptance is strongly affected by and can greatly change during the laser processing; changes in thermophysical properties of powder, particle rearrangement, phase transition and oxidation all influence absorptance. Also, absorptance is time and process dependent and generally the greater the absorptance power, the less the laser energy required.

### Solid–liquid interface properties

Among surface properties, surface tension is by far the most relevant when dealing with AM processes, because both in LS and LM phase transition occur and coexistence of solid and liquid is always present. The wetting behaviour of the molten system and the solidified processed layer is related to the surface tensions of solid–liquid (SL), solid–vapour(SV) and liquid–vapour (LV) by the Young's equation

$$\gamma_{SG} - \gamma_{SL} - \gamma_{LG} \cos \theta_C = 0, \quad (2.2)$$

where  $\theta_C$  is the contact angle. The main issue associated to a poor wettability of a system has been disclosed by Das [7]: since metals show a rather common tendency to surface passivation with the formation of oxides, the presence of this contamination layer on the surface of melts and on previously processed layer is a strong impediment to a good wettability and causes structural defects such as balling (see Section 1.2.2). Interface properties play an important role also for what regards phase transition, ubiquitous in any AM process. Studying how a phase transition occurs means being able to know what controls nucleation, which happens when the melt begins to cool down after the highly energetic interaction with the laser source, and the subsequent growth, which strongly affects the nature of the microstructure of the processed component. In this context, properties like the nucleation rate, the mechanism of the nucleation itself (e.g. planar or dendritic) and growth speed during solidification are of primary interest at the industrial level.

## 2.2 Focus on interfacial properties

During first-order phase transition such as nucleation and growth, interfacial properties play a central role. In particular, the interfacial free energy between the solid and the liquid phase (usually indicated with  $\gamma_{s1}$ ) controls the barrier for nucleation of solid in an undercooled liquid and the crystal growth, which can present different regimes: planar, cellular and dendritic, the latter of particular interest for metals.

---

<sup>1</sup>It should not be confused with absorbance, which is a more specific property of matter related to the intensity of incident beam of monochromatic light and the intensity of the radiation passed through the sample:  $A = \log_{10} I_0/I$ .

Despite its importance from both theoretical models and practical applications, an accurate calculation of  $\gamma_{sl}$  is a rather complicated task even for the case of simple elements. Furthermore, on the experimental side, few techniques aimed at measuring this quantity are complicated by the very strict control on all experimental parameters that must be achieved to obtain accurate data. One method, for example, involves recovering  $\gamma_{sl}$  from nucleation–rate measurements: in this particular case, a major difficulty arises from the possible occurrence of heterogeneous nucleation from very low-concentration of impurities.

Several computational methods have been developed to calculate  $\gamma_{sl}$ , where a complete control on the experimental variables is possible. These methods are the *capillary fluctuation method* (CFM), different sorts of so-called *cleaving methods* (CMs) and approaches based on *classical nucleation theory* (CNT). All these schemes largely rely on molecular dynamics in conjunction with Monte Carlo simulations.

Recently, approaches of this kind coupled with the accelerated sampling technique of metadynamics have been presented: the key idea is to obtain  $\gamma_{sl}$  from a free–energy map of the phase transition reconstructed by metadynamics [28], allowing also to investigate solidification and melting in out-of-equilibrium conditions [29], much more relevant for experiments and mesoscale models of solidification (including additive manufacturing processes).

### Overview of methods

In the following paragraphs we try to give a quick overview of the known methods for computing the solid–liquid interfacial free energy by means of molecular simulations. We will address more attention on CFM in the next section, on which we concentrated our efforts in the present research. A thorough description of the revisited method we adopted to obtain our results will be given in Chapter 3.

In CMs, bulk solid and liquid phases are separately cleaved along the surface of interest and the different phases are joined to form the interface. In this way,  $\gamma_{sl}$  is obtained by measuring the work done during the process [30, 31].

In the CNT approach, instead, crystalline nuclei of different sizes are introduced into a supercooled liquid phase and an orientational average of  $\gamma_{sl}$  can be calculated by measuring the radius of the critical nucleus  $R^*$  and inserting its value in the classical nucleation theory equation relating the critical radius and  $\gamma_{sl}$

$$R^* = \frac{2\gamma_{sl}}{\Delta G_{sl}}, \quad (2.3)$$

where  $\Delta G_{sl}$  is the difference in Gibbs free energy between bulk solid and liquid. For small undercooling,  $\Delta T$ , the latter term can be approximated with  $-\Delta S_f^m \Delta T$ , in which  $\Delta S_f^m$  is the molar entropy of fusion.

All these methods (including CFM) have been successfully applied to model systems such as hard spheres [30, 32] and Lennard–Jones potential [33, 34] as well as to more realistic semiempirical and quantum–mechanical systems modeled by embedded atom

model (EAM) [33] or Stillinger–Weber [35] potentials.

Both CFM and CNT have the disadvantage of being derived with approximations valid on the macroscale and for this reason require large simulation supercells with the order of  $10^5$  atoms to be applicable and give reliable results. Cleavage methods requires smaller system, but may introduce non negligible errors if the simulations performed are not completely reversible, for example if complete solidification of the liquid happens while joining it to the solid due to large relative fluctuations of the interface. Lastly, interface free energy have shown to be very sensitive to the details of the potential used. For instance, different parametrizations of EAM potentials yields values of  $\gamma_{sl}$  which vary by as much as 30% [36].

## 2.3 Capillary fluctuations and free energies

The capillary fluctuation method was firstly introduced by Asta and coworkers [37] in 2001 and employs an analysis of height fluctuations of the solid–liquid interface at equilibrium to extract the interface stiffness,  $\sigma$ .

In purely mathematical terms, the stiffness can be defined as the second–order coefficient of the power expansion of the free energy with respect to orientation. In this context, orientation means an instantaneous angle (or two of those if we deal with a 2D surface, as explained later) by which the normal of the interface is tilted with respect to the axes of the chosen coordinate system (usually a Cartesian system). From a physical point of view, the stiffness is related to the energy cost of bending the surface.

The approach of CFM has been successfully applied to derive interfacial free energies from atomistic simulations for the liquid–vapor surface of Lennard–Jones system [38] and for amorphous polymer films [39], just to mention a couple of examples.

The CFM starts with crystal–liquid systems that have been equilibrated at the melting point using molecular dynamics for pure materials or Monte Carlo simulations necessary to study alloys. To minimize the number of atoms, typical simulation cells are chosen to be quasi–two dimensional, with the length of the interface  $d$  much larger than the thickness of the system,  $b$  (see Fig. 2.1). The length  $d$  is chosen sufficiently large to allow measurement of capillary fluctuation amplitudes over a wide range of wavelengths.

Since periodic boundary conditions are applied, two identical interfaces are present in a simulation box. Thus, to avoid unwanted interactions between the two interfaces, the length of the simulation cell parallel to the interface normal is chosen to be of the order of  $2d$ .

In short, CFM is based upon collecting snapshots of the system during the simulation and for each of them measure the squared amplitude of capillary fluctuations. At the end of the simulation, an ensemble average is computed to obtain the mean value of the amplitudes: this term is directly related to the interfacial stiffness. In this context, the stiffness  $\sigma$  is defined as  $\gamma + \gamma''_\theta$ , where  $\gamma''_\theta$  denotes the second derivative of the interfacial free energy with respect to the orientational angle  $\theta$ , that is the angle between the local normal to the solid–liquid interface and the average orientation for the reference flat

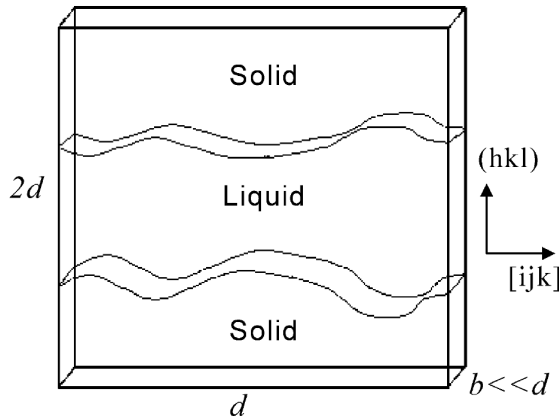


Figure 2.1 – Ref: Hoyt, Hasta and Karma CFM review.

interface. The key point of this approach is that the stiffness is one order of magnitude more anisotropic than the free energy itself, thus it can be computed more easily with smaller errors.

The CFM exploits the well-known result from capillary theory [40] for which the stiffness is directly related to the equilibrium fluctuation spectrum of a rough interface. In mathematical terms, for a quasi-two dimensional interface, this reads

$$\langle |A(k)|^2 \rangle = \frac{k_B T_m}{S(\gamma + \gamma''_\theta) k^2}, \quad (2.4)$$

where  $S$  is the cross sectional area of the interface and  $T_m$  the melting temperature.  $A(k)$  is the amplitude of an height perturbation of the interface with wavelength  $\lambda = 2\pi/k$  much larger than the lattice spacing. In other words, the terms denoted by  $A(k)$  for different wave vectors  $k$  are the coefficients of the Fourier expansion of the height function,  $h(x)$

$$h(x) = \sum_k A(k) \exp(ikx). \quad (2.5)$$

The quantities  $\gamma$  and  $\gamma''_\theta$  in the denominator of Eq. 2.4 originate from the energy cost of bending locally the interface away from its mean orientation, which is why the fluctuation spectrum measures directly the interface stiffness.

At this point, a fundamental question that arises is related to the method needed to construct the height function  $h(x)$ . To answer this question, one need to know a way of locating the interface during the simulation. To this end, the vast majority of scientific literature of CFM exploits some kind of local structural order parameter which is able to distinguish between solid and liquid atoms. Through the use of such order parameter, the position of the interface can be identified as a function of the distance along the interface (i.e.  $x$  in this one-dimensional case, but in the most general case, one would have a function  $h(x, y)$  of the two coordinates parallel to the interface). An in depth

### 2.3. Capillary fluctuations and free energies

---

description of the way we adopted to be able to distinguish solid and liquid phases and to locate the instantaneous position of the interface will be given in the next chapter. With the “recipe” given by Eq. 2.4 and Eq. 2.5, the CFM is used to derive values of the stiffness for several interface orientations and the results are then combined with an analytical expansion of the interface free energy  $\gamma(\hat{n})$  to map out the full anisotropy of the solid–liquid interfacial free energy. For the applications considered here, the appropriate expansion for  $\gamma(\hat{n})$  involves cubic harmonics, that are linear combinations of spherical harmonics that obey the cubic symmetry of the lattice. Following the approach developed by Fehlner [41], the expansion for the interface free energy is

$$\frac{\gamma(\hat{n})}{\gamma_0} = 1 + \epsilon \left( \sum_{i=1}^3 n_i^4 - \frac{3}{5} \right) + \delta \left( 3 \sum_{i=1}^3 n_i^4 + 66n_1^2 n_2^2 n_3^2 - \frac{17}{7} \right) + \dots \quad (2.6)$$

where  $\hat{n} = (n_1, n_2, n_3)$  is the interface normal and the parameters  $\epsilon$  and  $\delta$  give a measure of the anisotropy of  $\gamma$ .

With the relation of Eq. 2.4 and the expansion of Eq. 2.6, three different calculations for independent interfaces are needed to obtain the parameters of the expansion ( $\gamma_0$ ,  $\epsilon$  and  $\delta$ ). In a more recent work on dendritic growth in metals, Becker et al. [42] made use of different simulations geometries containing two-dimensional interfaces, instead of the so far discussed “quasi” two-dimensional. In this case, one must fully take into account the possibility of capillary waves also in the other direction parallel to the interface and the relation between amplitudes of capillary fluctuations and wave vectors becomes

$$\langle |A(k_x, k_y)|^2 \rangle = \frac{k_B T_m}{S(\sigma_{11} k_x^2 + \sigma_{22} k_y^2 + 2\sigma_{12} k_x k_y)}. \quad (2.7)$$

Although these 2D simulation geometries require larger cells and in turn more atoms, there is the advantage that from two independent interface normals (due to symmetry arguments, as explained in the following), three independent stiffness values can be obtained and so only two simulations are needed to fully parametrize  $\gamma$ . Moreover, more  $k$  modes are accessible from a 2D interface, because wave vectors have the form  $2\pi(j_1/L_1, j_2/L_2)$ , where  $L_1$  and  $L_2$  are the lengths of the simulation box along the interface and  $j_1, j_2$  are two non-zero indexes.

For 2D interfaces, the stiffness  $\sigma$  is a second-order tensor with three independent values in general<sup>2</sup>, but symmetry arguments can reduce the independent values for certain interface orientations. For example, for a (100) interface in a FCC crystal, if two of the Cartesian axes are along [100] and [010] directions, the off-diagonal terms are zero and the diagonal terms are equal. In this case, the general relation of Eq. 2.7 is similar

---

<sup>2</sup>This is true on general grounds because of the definition of the stiffness as second-order derivative of the interface free energy with respect to the orientational angles:

$$\sigma_{ij} = \frac{\partial^2 \gamma}{\partial \theta_i \partial \theta_j}.$$

to the equation for the 1D geometry, but it is important to stress that  $\gamma$  can still be parametrized with two independent interfaces: the fact that the stiffness tensor reduces to a single component is purely a consequence of symmetry.

# 3 The capillary fluctuation method revisited

As discussed in detail in the previous chapter (Section 2.3), the capillary fluctuations method is a technique that can be essentially divided in four “steps”.

1. **Defining an appropriate way to discriminate solid and liquid.** This is the very first step since the next goal will be that of “locating” in an atomistic system the dividing surface between the solid and the liquid phase.
2. **Analysing the surface profile.** At this point we are able to distinguish atoms that belong to a solid-like environment and liquid-like ones; we can track down the position of the surface by collecting snapshots of its profile,  $h$ . The latter is in general a function of two variables, i.e. the coordinates (with respect to the chosen coordinate system) in the interface plane. At the end of the simulation, the profile function  $h$  is Fourier transformed and an ensemble average is computed to obtain the so-called fluctuations spectrum.
3. **Fitting the fluctuations spectrum.** Relations such as Eqs. (2.4) and (2.7) give the explicit link between capillary fluctuations and surface stiffness  $\sigma$ . Through the fit of these non-linear models for different surfaces, we are able to completely determine the  $\sigma$  tensor.
4. **Extracting the anisotropy coefficients.** Since we know the relation between interface free energy and the stiffness and we have an approximation of the anisotropy of  $\gamma$ , we can analytically determine  $\sigma$  from Eq. (2.6) and fit this against the value of the stiffness calculated previously. In this way we will obtain the two anisotropy coefficients (here  $\epsilon$  and  $\delta$ ) and completely map out the dependence of  $\gamma$  from the interface orientation.

## 3.1 The method

In this section we explain in full detail all the aforementioned steps, which build the framework of capillary fluctuation method we adopted for our calculations of the stiffness for a Lennard-Jones system, devoting more attention to the substantial differences with the original method developed by Asta<sup>1</sup>.

---

<sup>1</sup>See footnote 12, pag. 19

### 3.1.1 Solid or liquid

As it has already been stressed, the very first requirement for a computational method whose aim is to study phase transitions or coexistence between different phases is a way of distinguishing particles belonging to the phases involved<sup>2</sup>.

In molecular simulations of this kind, it is widespread to make use of a more or less complicate function that depends on atomic coordinates and that can give a quantitative indication of the “order” of one atom’s neighborhood: this class of functions are usually called *order parameters*. Many of these functions have been developed in order to face different problems; probably, the most known order parameters are the *Steinhardt–Nelson* functions of different orders:  $Q_3$ ,  $Q_4$  and  $Q_6$  [43].

A common feature of all these order parameters is that they are some sort of average computed considering the coordinates of all the atoms and it should be intuitive that no function of this type is able to distinguish, for example, all the crystalline phases of a given system if they have different symmetry. In other words, a certain choice of an order parameter might be more suitable than another if one wants to study the environment of an HCP crystal rather than an FCC one. Since all our systems (Lennard–Jones and real metal alloys) show at least one FCC crystalline phase, we chose the order parameter adopted also by Angioletti–Uberti [28] and BCheng [29] in their metadynamics calculations of interface free energy. This order parameter (henceforth called **FCCUBIC**,  $\Phi$ ) is defined as

$$\Phi(\mathbf{x}_i) = \frac{\sum_{j \neq i} C_r(|\mathbf{x}_j - \mathbf{x}_i|) C_\alpha(\mathbf{x}_j - \mathbf{x}_i)}{\sum_{j \neq i} C_r(|\mathbf{x}_j - \mathbf{x}_i|)}. \quad (3.1)$$

The **FCCUBIC** order parameter is a weighted average running over all pairs of atoms of an angular term ( $C_\alpha$ ) and a “weight” which is a radial cutoff function ( $C_r$ ) that ensures that  $\Phi$  is a continuous function of all its arguments. The angular part can be specified using a set of Euler angles (by means of a Euler rotation matrix  $\mathbf{R}$ ) and can be written as

$$C_\alpha^{(\varphi, \psi, \theta)}(\mathbf{r}_{ij}) = C_\alpha(\mathbf{R}^{(\varphi, \psi, \theta)} \cdot \mathbf{r}_{ij}). \quad (3.2)$$

Advantages of **FCCUBIC** order parameter over the mentioned Steinhardt’s Q functions are, mainly: the angular part  $C_\alpha$  has well-defined peaks for the FCC environment; it is not rotationally invariant and thus it is be able to recognize crystal orientations consistent with the imposed periodic boundary conditions; it is relatively cheap to compute. It is be possible to construct a different form of  $C_\alpha$  if one wanted to deal with a different crystal structure, and one simply has to rotate the function through the Euler matrix  $\mathbf{R}$  in order to specify a different crystallographic orientation of the surface. The possibility of having an orientation-dependent order parameter is an essential ingredient of our method.

---

<sup>2</sup>Here we restrict ourselves to the case of solid and liquid, but it is clear that this prerequisite is completely general.

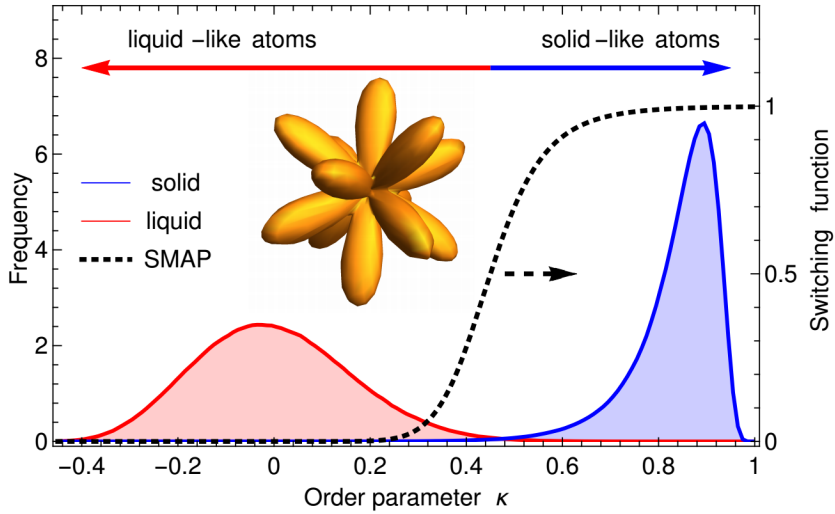


Figure 3.1 – The distributions of the FCCC order parameter for a bulk FCC crystal oriented with  $\langle 100 \rangle$  directions parallel to the axes of the simulation cell. The distributions are computed at the equilibrium melting temperature. The dashed line is a plot of the switching function applied [29].

The “final”  $\Phi$  actually used in our simulations is subject to few other mathematical manipulations mainly aimed to obtain that the perfect FCC lattice corresponds to  $\Phi = 1$ , while the average value for atoms in bulk liquid is zero<sup>3</sup>. Lastly, since the distributions of such order parameter for a bulk solid system and a bulk liquid have a minimal amount of overlap (see Fig. 3.1), a non-linear switching function is applied to  $\Phi$  in order to have a tunable and smooth variation from solid-like region to liquid-like<sup>4</sup>.

### 3.1.2 Looking for the dividing surface

In the work of Asta et al. they obtained the profile function of the dividing surface in the following way: they computed an FCC order parameter defined as  $\phi = (1/12) \sum_i |\mathbf{r}_i - \mathbf{r}_{fcc}|^2$ , where  $\mathbf{r}_{fcc}$  is the distance between the central atom  $i$  and its first 12 neighbours in the given orientation. Then, the  $x$  direction in the simulation cell, parallel to the interface, is divided into slices and  $\phi$  averaged over the slice is computed as a function

<sup>3</sup>This is ensured by applying a linear scaling of the kind

$$\Phi(i) = \frac{\Phi^0(i) - \Phi_l^0}{\Phi_s^0 - \Phi_l^0},$$

where  $s$  and  $l$  indicate the average of  $\Phi$  on a bulk solid and liquid system respectively, and  $\Phi^0$  is the unscaled order parameter defined above.

<sup>4</sup>In this case, the non-linear switching function applied has the form

$$s(r) = \left[ 1 + (2^{a/b} - 1) \left( \frac{r - d_0}{r_0} \right)^a \right]^{-b/a},$$

where  $r_0$  and  $d_0$  are tunable parameters. For  $r \leq d_0$   $s(r) = 1$ , while for  $r > d_0$  the function decays smoothly to 0.

of the  $y$  direction (along the normal of the interface). As the solid–liquid interface is crossed, the value of  $\phi$  changes abruptly and the interface can be accurately located. By collecting snapshots of this function during all the simulation, one ends up with the time-varying profile function  $h(y, t)$ , where both the space and time coordinates are discretized.

The discrete nature of the profile function stems directly from the fact that the order parameter is a discrete quantity, since it assigns a numerical value to each atom. In turn, it means that the representation of the surface built in this way is highly sensitive on the  $x$ -width of the slices over which  $\phi$  is averaged (i.e. the bin size).

In our approach, we followed the idea proposed by Willard and Chandler [44]. To identify the liquid–vapour interface in water systems such that the resulting surface is to all effects a continuous function, they built a coarse-grained density field by computing the convolution of the instantaneous density field with a chosen kernel function. In this case, the kernel functions are taken to be normalized Gaussians, which depend on one parameter ( $\xi$ , the Gaussian width). So, in mathematical terms,

$$\begin{cases} \rho(\mathbf{r}, t) = \sum_i \delta(\mathbf{r} - \mathbf{r}_i(t)) \\ \kappa(\mathbf{r}; \xi) = (2\pi\xi^2)^{-d/2} \exp(-r^2/2\xi^2) \end{cases} \xrightarrow{\text{convolution}} \bar{\rho}(\mathbf{r}, t) = \sum_i \kappa(|\mathbf{r} - \mathbf{r}_i(t)|; \xi) \quad (3.3)$$

Here  $r$  is the magnitude of the distance vector  $\mathbf{r}$  and  $\xi$  is the coarse-graining length;  $d$  stands for the dimensionality of the system. As we will discuss in the Results section, the importance of  $\xi$  is that it controls the coarse nature of the continuous field obtained and it has to be chosen according to physical conditions under consideration.

From this idea for a simple density field to an *order parameter density field*, the step is really short: it suffices modifying the instantaneous atomistic “density” as follows

$$\rho(\mathbf{r}, t) \rightsquigarrow \rho_\phi(\mathbf{r}, t) = \sum_i \phi_i \delta(\mathbf{r} - \mathbf{r}_i(t)), \quad (3.4)$$

and the coarse-grained field needs to be properly normalized

$$\bar{\rho}_\phi(\mathbf{r}, t) = \frac{\sum_i \phi_i \kappa(|\mathbf{r} - \mathbf{r}_i(t)|; \xi)}{\sum_i \kappa(|\mathbf{r} - \mathbf{r}_i(t)|; \xi)}. \quad (3.5)$$

Once  $\xi$  is set, the dividing surface is defined to be the  $(d - 1)$ -dimensional manifold  $\mathbf{r} = \mathbf{s}$  for which

$$\bar{\rho}_\phi(\mathbf{s}, t) = C, \quad (3.6)$$

where  $C$  is some constant value. In other words, the instantaneous interface between solid and liquid is the locus of points in space where the order parameter density field assumes the value of  $C$  (sometimes called *isovalue*). It is clear that the choice of this constant is arbitrary, but it should rely on some meaningful physical consideration. Since the coarse-grained field changes with time as molecular configurations change,

the surface is a two-dimensional function which depends on time only through atomic coordinates:  $\mathbf{s}(t) = \mathbf{s}(\{\mathbf{r}_i(t)\})$ .

For a given molecular configuration  $\{\mathbf{r}_i\}$  at time  $t$ , Eq. (3.6) can be solved quickly with a variety of numerical algorithms, for example through interpolation on a spatial grid. If this equation is recast in the form  $\bar{\rho}_\phi(\mathbf{r}, t) - C = 0$ , one among all the known root-finding algorithms can be exploited to solve it. We adopted the method due to Brent and Dekker<sup>5</sup>, which has the reliability of the bisection method, but it is faster in convergence.

Once an entire simulation for a specific interface is analysed, the interface profile function is Fourier transformed to obtain its fluctuation spectrum. Practical details of the simulations will be given in the next section; here it is sufficient to note that we employed the 2D geometry so that we needed only two independent surfaces to get the full anisotropy through the stiffness tensor. To get fluctuations amplitudes that appears in Eq. (2.7),  $h(\mathbf{x})$ , where  $\mathbf{x}$  is the vector with components  $(x, y)$ , is Fourier transformed according to

$$h(\mathbf{x}, t) = \sum_{\mathbf{k}} A(\mathbf{k}, t) \exp(i\mathbf{k} \cdot \mathbf{x}), \quad (3.7)$$

and  $\mathbf{k}$  is the wave vector which takes the form  $2\pi(j_x/L_x, j_y/L_y)$ , with  $j_x, j_y$  being non zero indexes and  $L_x, L_y$  the size of the simulation cell in the interface plane.

The last step is to compute the ensemble (time) average of the fluctuation spectrum<sup>6</sup>, where with “spectrum” we refer to the square moduli of the complex Fourier amplitudes.

One last detail is necessary to discuss: how to fix the constant value  $C$  in order to solve Eq. (3.6). In the original paper where this method was introduced, the authors were using the method to provide useful and instructive pictures of liquid-vapour and liquid-protein interfaces, particularly with water. For the case of the liquid-vapour dividing surface, they fixed the constant to one-half the density of liquid water in their system.

In our case, a physically reasonable value for the constant would be the one that could clearly discriminate between a particle in a solid-like environment from one in the liquid-one. Unfortunately, as one can see from Fig. 3.1, there is no such sharp value. So, we firstly chose as  $C$  the average value of the order parameter between an all solid system and an all liquid one, namely:  $(\Phi_s + \Phi_l)/2$ . However, we realized that such value was susceptible of appreciable changes if the interface was moving considerably due to fluctuations (larger in smaller cells) or if we changed the coarse-graining length  $\xi$ . Hence, we had the idea of transforming again the order parameter function by

---

<sup>5</sup>See [https://en.wikipedia.org/wiki/Brent%27s\\_method](https://en.wikipedia.org/wiki/Brent%27s_method)

<sup>6</sup>Again, practical details on how this average has been calculated will be given when discussing results. Here we just note that, since time is discretized by definition in a MD simulation, we only have snapshots of the fluctuation spectrum and the time interval between two of these is a multiple of the timestep used in the MD simulation. Since an observable in consecutive snapshots may show a correlated behaviour, we exploited a way of computing the average in order to estimate correctly also the error on this average.

applying a second switching function: this function (see Footnote 4) was tuned so that the resulting order parameter had a really sharp change when traversing the diving surface; in this way, liquid atoms had a value of  $\Phi$  very close to 0 and solid ones almost equal to 1. We could then fix the value of the constant to 0.5<sup>7</sup>.

### 3.1.3 Fitting capillary fluctuations spectrum

To obtain the values of the stiffness tensor  $\sigma$ , the only thing left is fitting the averaged fluctuation spectrum with respect to  $k$ -vector, following the prescription of Eq. (2.7):  $T_m$  is known and the cross sectional area  $S$  is simply the product  $L_x \times L_y$ . The only substantial difference here is a multiplicative term added to the fitting model, which changes into

$$\langle |A(k)|^2 \rangle = \mathcal{P} \frac{\exp(-k^2/2\xi^2)}{k_x^2 \sigma_{11} + k_y^2 \sigma_{22} + 2k_x k_y \sigma_{12}}, \quad (3.8)$$

where  $\mathcal{P} = k_B T_m / S$  is the constant prefactor. To explain why we added the exponential term, we recall that our representation of the surface is the result of a convolution of a Gaussian function with the order parameter density field. It is known that the Fourier transform of a convolution is the pointwise product of Fourier transforms and the Fourier transform of a Gaussian is again a Gaussian with a different width: this is the reason behind our modification of the fitting model.

---

<sup>7</sup>Another small, but important detail hides in here: when computing the field as in Eq. (3.5), the distance  $|\mathbf{r} - \mathbf{r}_i|$  refers to a certain coordinate system with a fixed origin. It should be evident that changing the origin will influence the final result for  $\rho_\phi$ . So, in all our analysis, we fixed the origin by computing a weighted average position based on the values of the order parameter. Coordinates of the origin are defined according to

$$x_\alpha = \frac{1}{2\pi} \arctan \left[ \frac{\sum_i w_i \Phi_i \sin(2\pi x_{i,\alpha})}{\sum_i w_i \Phi_i \cos(2\pi x_{i,\alpha})} \right],$$

where  $w_i$  are weights,  $\Phi_i$  are the values of the order parameter and  $x_{i,\alpha}$  the scaled Cartesian components of the position of the atoms. All the analysis were run within the framework of the software PLUMED, with which is rather easy to compute such a quantity.

# 4 Modeling atomistic interactions

## 4.1 The embedded atom method

In recent years, our knowledge of the atomic structure of solids and their physical properties has advanced considerably both from theoretical and experimental points of view. More versatile and powerful methods in computational science allowed the possibility of investigate more deeply properties and phenomena of condensed matter; this has been possible also thanks to the growing computers' power. From the experimental side, it is now possible to resolve with very high accuracy the atomic scale structure of complex system like interfaces, surfaces, and grain boundaries. Lastly, but not less important, the broad class of first principles calculations, such as the well-known density functional theory, are capable of explaining complex and basic properties that years ago were only took into account as approximations.

Despite all this huge progress, many systems of interest for a variety of scientific fields are still too complex and demand reliable but approximate methods. All the relevant properties of matter in any of its forms arise from the interactions among its constituents, be them atoms, molecules or macromolecules such as proteins or polymers. A unique way of explaining all these possible interactions is both impossible and useless, because one would have to deal with an enormous quantity of informations.

The very first approach to model interactions involves the class of pair potentials (the Lennard-Jones potential is the easiest example). Although this potentials can be useful to model very simple system or to give a rough approximation of some kind of fundamental interaction, the pair potential scheme has been shown to fail in describing the physics of metallic bonding. This kind of interaction is undoubtedly a fundamental one because of the vast numbers of elements and compounds that show metallic behaviour.

Most of the questions regarding structure and thermodynamics of condensed matter system can be answered from the knowledge of the total energy. The total energy of a solid can be determined, at least in principle, by solving the many-electron Schrödinger equation, but this problem is overwhelming in practice and some approximations are needed to reduce the complexity without loosing the important physics. The scheme of pair interactions is clearly the most extreme approximation and it easy to show why

it falls short. If we take the cohesive energy to be a sum only over pair bonds,

$$E_{coh} = \frac{1}{2} \sum_{i \neq j} V(R_{ij}), \quad (4.1)$$

it is evident that bonds between atoms are independent of each other. This assumption is very simple and can be also very useful, but it has the major difficulty that it is not possible to show theoretically that the total energy can be written as a sum over pairs. The error stems from the fact that, in general, bonds between atoms are not independent of each other. To be more concrete, it is sufficient to look at a table of cohesive energy measured experimentally for crystal structures that differ only by the coordination  $Z$  of a typical atom: the pair model of Eq. (4.1) predicts that the cohesive energy scales linearly with  $Z$  ( $E_{coh} \propto -Z$ ), but in reality the energy scales more weakly with a power law like  $-Z^{1/2}$ : this means that the strength of an additional bond is not constant, but rather decreases with increasing  $Z$ .

The very simple argument stated above seems to suggest that the key to understand many of the interesting problems in the structure of solids (and in particular of metals) lies in coordination-dependent interactions. It was with this idea in mind that Daw and Baskes in 1983 [45, 46] proposed the *embedded atom model* (EAM). In this scheme, the total energy of a metal is a sum of energies obtained by inserting an atom into the local electron density produced by the remaining atoms of the system. Since we are dealing with charged particles, there is an additional pair term that takes into account electrostatic interaction. The expression for the total energy  $E_i$  of the  $i$ -th atom within EAM is

$$E_i = F_\alpha \left( \sum_{j \neq i} \rho_\beta(r_{ij}) \right) + \frac{1}{2} \sum_{j \neq i} \phi_{\alpha\beta}(r_{ij}). \quad (4.2)$$

Here  $F$  is the embedding energy, defined as the interaction of the atom  $i$  of type  $\alpha$  with the background electron gas;  $\rho_\beta$  is the spherically averaged atom electron density and  $\phi$  is an electrostatic, two-atom interaction. The background density for each atom is determined by evaluating at its nucleus the superposition of atomic density tails from the other atoms.

In 1984, Finnis and Sinclair [47] proposed a more general way of computing the total energy term  $E_i$ ,

$$E_i = F_\alpha \left( \sum_{j \neq i} \rho_{\alpha\beta}(r_{ij}) \right) + \frac{1}{2} \sum_{j \neq i} \phi_{\alpha\beta}(r_{ij}). \quad (4.3)$$

This has the same form as Eq. (4.2), except that  $\rho$  is now a functional specific to the atomic types of both atoms  $i$  and  $j$ . In this way distinct elements can contribute differently to the total electron density at an atomic site depending on the chemical

species of the element at that particular atomic site.

One interesting aspect of EAM is its physical description of the metallic bonding: each atom is embedded in an host electron gas created by its neighboring atoms. The atom–host interaction is inherently more complex than the simple two-body picture of the pair-bond model. In this way the embedding functions  $G$  can incorporate some important effects which arise only from considering many-body interactions.

Currently, EAM is the first choice for doing semi-empirical calculations in close-packed metals and related compounds such as alloys. The EAM combines the computational simplicity needed for large systems with a physical description of the underlying interactions that includes many-body effects, which are completely ignored in a pair-bond model.

To conclude this very quick theoretical overview of EAM, in the review work of Das, Foiles and Baskes [48] a series of examples for which the EAM has been successfully applied are cited and thoroughly discussed.

## 4.2 Applications to alloys

EAM potentials have been applied to study various properties of alloyed metals, such as the compositional variations that can occur near defects. The main advantage of EAM over other approaches is that the interaction of one atom with the electron gas does not depend on the origin of the latter, but it is rather assumed to depend only on the local electron density. A change in the chemical identity of the neighbors enters the problem through a change in the electron densities (i.e. the functions  $\rho^a$ ); this means that the embedding function used for pure metals should still be valid for the case of alloys.

One should also be aware of possible errors when applying EAM potentials to complex systems like alloys. Large charge transfers in an alloy will be poorly described in the EAM, as well any effect arising from subtleties of the Fermi surface, that are completely ignore in the EAM.

This section will present some useful and recent applications of the EAM to study different properties of metal alloys, with a particular focus on nickel and gold alloys.

### 4.2.1 Nickel ternary alloys

As described previously, Ni-based superalloys are subject of many studies for their high performance applications as structural materials with excellent strength and creep resistance. These alloys are generally made of Ni, Ti and Al and the precipitation of the  $\gamma'$  ordered phase within the Ni FCC matrix is mainly responsible for the high strength. Also, plasticity response is thought to be due to formations of defects such as vacancies and impurities that affect dislocations motion. For all these reasons, it is interesting to have a method to simulate and understand the underlying processes on the atomic-scale.

The study of nickel ternary alloys typically requires reliable potentials to model interactions between Ni-Al, Ni-Ti and Al-Ti. The Ni-Al system has been widely studied and

several EAM potentials have been developed [49], based both on the Ni<sub>3</sub>Al system [50, 51] and on NiAl system [52, 53]. For this ternary system some complication arise from the Ti–Al case, for which the EAM fails in reproducing correctly the elastic constants due to the presence of non central forces<sup>1</sup>. Farkas [54] has developed and compared interatomic potentials for the Ti–Al system that included the non–central terms as well as a best possible potential without the angular term. In that work, Farkas showed that the main contribution of including central interactions was in the elastic constants, while total energy and stacking faults energies of various phases of Ti–Al system varied much less.

When dealing with alloys of three (or even four) components, the EAM presents a practical advantage: the pairwise term involves only two atoms at a time and therefore can be calculated from the binary interactions involved in the ternary system in question. The embedding functions are defined separately for each of the components of the system and does not require any additional fitting beyond that done for pure components. Also the local electronic density depends only on the strength of each individual contributions of each of the three components. It follows that if EAM potentials are available for the three binary systems involved in a particular ternary, it is in theory possible to describe also the ternary system. The only requirement is that the interatomic interaction used for each of the pure components in the description of the two binaries involving that constituent be the same.

In the work of Mishin in 2004 [55], a new EAM potential has been developed for the Ni<sub>3</sub>Al system, by fitting to both experimental and first–principles data. A series of recent works, aimed also to understanding the role of defects formation in plasticity response of Ni ternary alloys [56], have considered this new potential to be among the most reliable ones for modeling  $\gamma + \gamma'$  phases on Ni superalloys, with good accuracy in predicting  $\gamma/\gamma'$  interface energy.

Lastly, a ternary potential for the system Ni–Al–W has been constructed by Fan et al. [57] for the Ni-based single crystal superalloys to model the doping of Ni–Al system with tungsten, also comparing results with other calculations when the doping element were Re or Co<sup>2</sup>.

Results obtained with this potential were in good agreement with experiment; for example, the potential predicts that the solute atoms of W does not form cluster within the  $\gamma$  phase, which is consistent with experiments. Also, increasing the addition of W, the lattice misfit between the two phases decreases and the elastic constants of the  $\gamma'$  phase increase.

To conclude this part on EAM applied to Ni and alloys, two tables are reported: the first one summarizes the results of Mishin [55] on lattice properties of Ni and Al calculated with the EAM potential there developed; in the table are also present experimental data [58–60]. The second one shows the predicted equilibrium energies

---

<sup>1</sup>Ref. 6 ibidem

<sup>2</sup>W, Re, Co, Mo and Va are common additives for Ni superalloys since they behave as solid–solution strengtheners both for  $\gamma$  and  $\gamma'$  phases.

## 4.2. Applications to alloys

---

Table 4.1 – Lattice properties of Ni and Al calculated with the potential developed by Mishin [55] in comparison with experimental data.

Property	Ni		Al	
	Experiment	EAM	Experiment	EAM
$a_0$ (nm)	0.352	0.352	0.405	0.405
$E_0$ (eV)	-4.45	-4.45	-3.36	-3.36
<i>Elastic constants (GPa):</i>				
B	181.0	181.0	79.0	79.0
$c_{11}$	246.5	241.3	114.0	116.8
$c_{12}$	147.3	150.8	61.9	60.1
$c_{44}$	124.7	127.3	31.6	31.7

of different structures of Ni and Al with the EAM potential of Mishin, in comparison with first-principles calculations.

### 4.2.2 Gold and its alloys

Literature on EAM potential on gold and related alloys is less numerous than nickel (or titanium), especially when going beyond the simple metal system. Nevertheless, as we explained previously, the EAM framework allows to combine different single-element potentials, that should reproduce as best as possible the interested properties, and build from these an effective potential for the complex system under study, for example a ternary alloy.

With this in mind, the table below is taken from the recent work of Grochola et al. [61], in which a new EAM potential for gold is developed, using an improved methodology to fit to high-temperature solid lattice constants and liquid densities. This new potential shows an appreciable overall improvement in the agreement with several experimental data, in comparison with previous potentials of Foiles et al. [62], Johnson [63] and the glue model potential of Ercolessi et al [64]. Grochola and coworkers emphasize how

Table 4.2 – Equilibrium energies (in eV) for different stable structures of Ni and Al predicted by the EAM potential developed by Mishin [55], compared to first-principles calculations.

Structure	Ni		Al	
	Ab initio	EAM	Ab initio	EAM
HCP	0.03	0.03	0.04	0.03
BCC	0.11	0.07	0.09	0.09
L1 <sub>2</sub>	0.66	0.54	0.27	0.33
SC	1.00	0.72	0.36	0.30
Diamond	1.94	1.42	0.75	0.88

## Chapter 4. Modeling atomistic interactions

---

Table 4.3 – Comparison table between predicted values of EAM potentials for gold discussed (and referenced) in this section. The table is partially reproduced from Grochola et al [61]. Units: elastic constants in GPa, energies in eV and lattice parameters in Å.

Property	Potential developed by				
	Grochola	Ercolassi	Johnson	Foiles	Exp.
Cohesive energy	-3.924	-3.78	-3.930	-3.927	-3.93
Lattice constant	4.0701	4.0704	4.0806	4.0805	4.07
Bulk modulus	1.8026	1.8037	1.6987	1.6673	1.803
$c_{11} - c_{12}$	0.3207	0.5998	0.2687	0.2454	0.319
$c_{44}$	0.4594	0.5998	0.4069	0.4524	0.454
Melting point (K)	1159	1338	1053	1121	1337

attempting a fit to *all* the properties for which an experimental data is available is by far unsuccessful. However, the results obtained for gold suggest that for other metal species further overall improvements in potentials may still be possible within the EAM framework with an improved fitting methodology.

- [1] Y. F. Shen D. D. Gu and Z. J. Lu. In: *Mater. Des.* 30 (2009), pp. 2099–2107.
- [2] A. Blatter P. Fischer V. Romano and H. P. Weber. In: *Laser Phys. Lett.* 2.48–55 (2005).
- [3] T. Kaiser and G. J. Albrecht. In: *Laser Techn. J.* 4 (2007), pp. 54–57.
- [4] M. Agarwala et al. In: *Rapid Prototyp. J.* 1 (1995), pp. 26–36.
- [5] K. Kempen et al. In: *Solid Freeform Fabrication Symposium Proceedings* (2013).
- [6] C. Y. Yap et al. “Review of selective laser melting: Materials and applications”. In: *Appl. Phys. Rev.* 2.4 (2015). issn: 19319401. doi: 10.1063 / 1.4935926. url: <http://dx.doi.org/10.1063/1.4935926>.
- [7] S. Das. In: *Adv. Eng. Mater.* 5 (2003), pp. 701–711.
- [8] P. Fischer et al. “Microstructure of near-infrared pulsed laser sintered titanium samples”. In: *Appl. Phys. A Mater. Sci. Process.* 78.8 (2004), pp. 1219–1227.
- [9] B. V. Krishna, S. Bose, and A. Bandyopadhyay. In: *Acta Biomater.* 3 (2007), pp. 997–1006.
- [10] W. C. Xue et al. In: *Acta Biomater.* 3 (2007), pp. 1007–1018.
- [11] F. Abe et al. “The manufacturing of hard tools from metallic powders by selective laser melting”. In: *J. Mater. Process. Technol.* 111.1-3 (2001), pp. 210–213.
- [12] C Leyens and M Peters. *Titanium and titanium alloys*. Wiley VCH, 2003.
- [13] H. Okamoto and T. B. Massalski. *Phase Diagrams of Binary Gold Alloys*. ASM International, 1987.
- [14] A. Prince, G. V. Raynor, and D. S. Evans. *Phase Diagrams of Ternary Gold Alloys*. The Institute of Metals, 1990.
- [15] G. Effenberg and S. Ilyenko, eds. *Ternary Alloy Systems, Subvolume B: Noble Metal Systems*. Springer-Verlag, 2006.
- [16] J. P. Nielsen and J. J. Tuccillo. “Grain size in cast gold alloys”. In: *J. Dent. Res.* (1966).
- [17] D. Ott and Ch. J. Raub. “Grain size of gold and gold alloys”. In: *Gold Bulletin* 14(2) (1981), p. 69.

## Bibliography

---

- [18] F. J. Humphreys and M. Hatherly. *Recrystallization and Related Annealing Phenomena*. Elsevier, 2004.
- [19] K. Lücke and K. Detert. "A quantitative theory of grain-boundary motion and recrystallization in metals in the presence of impurities". In: *Acta Metall.* 5 (1957), p. 628.
- [20] *Edelmetalltaschenbuch (Precious Metal Pocketbook)*. Hüttig–Verlag, 1995.
- [21] C. Chaston. "Heat treatment of gold alloys: The mechanism of disorder order hardening". In: *Gold Bull.* 4 (1971), p. 70.
- [22] J. -J. Laberge, D. Tréheux, and P. Guiraldeng. "Hardening of gold-based dental casting alloys: Influence of minor additions and thermal ageing". In: *Gold Bull.* 12(2) (1979), p. 45.
- [23] R. Süss et al. "Carat yellow gold alloys with increased hardness". In: *Gold Bull.* 37(3–4) (2004), p. 196.
- [24] D. Becker, W. Meiners, and K. Wissenbach. "Additive manufacturing of copper alloys by selective laser melting". In: *Lasers in Manufacturing*. WLT, June 2009, pp. 195–199.
- [25] J. P. Kruth et al. "Selective laser melting of iron-based powder". In: *J. Mater. Process. Technol.* 149.1-3 (2004), pp. 616–622. ISSN: 09240136. doi: 10.1016/j.jmatprot.2003.11.051.
- [26] A. Simchi, F. Petzoldt, and H. Pohl. In: *J. Mater. Process. Technol.* 141 (2003), pp. 319–328.
- [27] I. Takamichi and I. L. G. Roderick. *The physical properties of liquid metals*. Clarendon Press, 1993.
- [28] S. Angioletti-Uberti et al. "Solid–liquid interface free energy through metadynamics simulations". In: *Phys. Rev. B* 81 (2010), p. 125416.
- [29] Bingqing Cheng, Gareth A. Tribello, and Michele Ceriotti. "Solid-liquid interfacial free energy out of equilibrium". In: *Phys. Rev. B - Condens. Matter Mater. Phys.* 92.18 (2015), pp. 1–5. doi: 10.1103/PhysRevB.92.180102.
- [30] J. Q. Broughton and G. H. Gilmer. In: *J. Chem. Phys.* 74 (1986), pp. 57–59.
- [31] R. L. Davidchack and B. B. Laird. In: *Phys. Rev. Lett.* 85 (2000), p. 4751.
- [32] J. R. Morris R. L. Davidchack and B. B. Laird. In: *J. Chem. Phys.* 125 (2006), p. 094710.
- [33] X.-M. Bai and M. Li. In: *J. Chem. Phys.* 124 (2006), p. 124707.
- [34] J. R. Morris and X. Song. In: *J. Chem. Phys.* 119.3920 (2003).
- [35] S. L. Altmann and A. P. Cracknell. In: *Rev. Mod. Phys.* 37 (1965), p. 19.
- [36] J. R. Morris, M. Mendelev, and D. Srolovitz. In: *J. Non-Cryst. Solids* 353.3565 (2007).

---

## Bibliography

- [37] J. J. Hoyt, Mark Asta, and Alain Karma. "Method for Computing the Anisotropy of the Solid-Liquid Interfacial Free Energy". In: *Phys. Rev. Lett.* 86 (24 June 2001), pp. 5530–5533. doi: 10.1103/PhysRevLett.86.5530. URL: <http://link.aps.org/doi/10.1103/PhysRevLett.86.5530>.
- [38] S.W. Sides, G.S. Grest, and M.D. Lacasse. In: *Phys. Rev. E* 60 (1999), p. 6708.
- [39] T. Hapke, G. Patzold, and D.W. Heermann. In: *J. Chem. Phys.* 109 (1998), p. 10075.
- [40] Alain Karma. "Fluctuations in solidification". In: *Phys. Rev. E* 48.5 (1993), pp. 3441–3458. issn: 1063651X. doi: 10.1103/PhysRevE.48.3441.
- [41] W.R. Fehlner and S.H. Vosko. In: *Can. J. Phys.* 54 (1976), p. 2159.
- [42] C A Becker et al. "Atomistic Underpinnings for Orientation Selection in Alloy Dendritic Growth". In: 125701.March (2007), pp. 98–101. doi: 10.1103 / PhysRevLett.98.125701.
- [43] P. J. Steinhardt, D. R. Nelson, and M. Ronchetti. In: *Phys. Rev. B* 28 (1983), p. 784.
- [44] Adam P Willard and David Chandler. "Instantaneous liquid interfaces". In: *J. Phys. Chem. B* 114.5 (2010), pp. 1954–1958. issn: 15206106. doi: 10.1021/jp909219k. arXiv: 0909.4761.
- [45] M.S. Daw and M.I. Baskes. In: *Phys. Rev. Lett.* 50 (1983), p. 1285.
- [46] M.S. Daw and M.I. Baskes. In: *Phys. Rev. B* 29 (1984), p. 6443.
- [47] M. W. Finnis and J. E. Sinclair. "A simple empirical N-body potential for transition metals". In: *Philosophical Magazine A* 50.1 (1984), pp. 45–55. doi: 10.1080 / 01418618408244210. eprint: <http://dx.doi.org/10.1080/01418618408244210>. URL: <http://dx.doi.org/10.1080/01418618408244210>.
- [48] Murray S. Daw, Stephen M. Foiles, and Michael I. Baskes. "The embedded-atom method: a review of theory and applications". In: *Mater. Sci. Reports* 9.7-8 (1993), pp. 251–310. issn: 09202307. doi: 10.1016/0920-2307(93)90001-U.
- [49] R Pasianot et al. In: *Modelling Simulation Mater. Sci. Eng.* 2 (1994), p. 383.
- [50] S M S. Foiles and Murray S. Daw. In: *J. Mater. Res.* 2 (1987), p. 5.
- [51] A. Voter and S. Chen. "Accurate interatomic potentials for Ni, Al and Ni<sub>3</sub>Al". In: *Materials Research Society Symp.* Vol. 82. 1987, pp. 175–180.
- [52] D. Farkas et al. In: *Modelling Simulation Mater. Sci. Eng.* 3 (1995), p. 201.
- [53] A. Rao, C. Woodward, and T. Parthasarathy. "Empirical interatomic potentials for L10 TiAl and B2 NiAl". In: *Materials Research Society*. Vol. 213. 1991, pp. 125–130.
- [54] D. Farkas. "Interatomic potentials for Ti-Al with and without angular forces". In: *Model. Simul. Mater. Sci. Eng.* 2 (1994), pp. 975–984.
- [55] Y. Mishin. "Atomistic modeling of the  $\gamma$  and  $\gamma'$ -phases of the Ni-Al system". In: *Acta Mater.* 52.6 (2004), pp. 1451–1467. issn: 13596454. doi: 10.1016/j.actamat.2003.11.026.

## Bibliography

---

- [56] F Bianchini, J R Kermode, and A De Vita. "Modelling defects in Ni-Al with EAM and DFT calculations". In: *Model. Simul. Mater. Eng.* 045012 (2016), p. 45012. issn: 0965-0393. doi: 10.1088/0965-0393/24/4/045012. url: <http://dx.doi.org/10.1088/0965-0393/24/4/045012>.
- [57] Qin Na Fan et al. "A ternary Ni-Al-W EAM potential for Ni-based single crystal superalloys". In: *Phys. B Condens. Matter* 456 (2015), pp. 283–292. issn: 09214526. doi: 10.1016/j.physb.2014.09.012. url: <http://dx.doi.org/10.1016/j.physb.2014.09.012>.
- [58] R.C. Weast, ed. *Handbook of chemistry and physics*. CRC Press, 1984.
- [59] G. Simmons and H. Wang. *Single crystal elastic constants and calculated aggregate properties*. MIT Press, 1977.
- [60] *Metals: phonon states, electron states, and Fermi surfaces*. Landolt-Bornstein, Springer, 1981.
- [61] G. Gschlösser, S. P. Russo, and I. K. Snook. "On fitting a gold embedded atom method potential using the force matching method." In: *J. Chem. Phys.* 123.20 (2005), p. 204719.
- [62] S. M. Foiles, M. I. Baskes, and M. S. Daw. "Embedded-atom-method functions for the fcc metals Cu, Ag, Au, Ni, Pd, Pt, and their alloys". In: *Phys. Rev. B* 33 (12 June 1986), pp. 7983–7991.
- [63] R. A. Johnson. "Analytic nearest-neighbor model for fcc metals". In: *Phys. Rev. B* 37 (8 Mar. 1988), pp. 3924–3931. doi: 10.1103/PhysRevB.37.3924. url: <http://link.aps.org/doi/10.1103/PhysRevB.37.3924>.
- [64] F. Ercolessi, M. Parrinello, and E. Tosatti. "Simulation of gold in the glue model". In: *Philosophical Magazine A* 58.1 (1988), pp. 213–226.